Chinese Chemical Letters 37 (2026) 111982

Contents lists available at ScienceDirect

Chinese Chemical Letters

journal homepage: www.elsevier.com/locate/cclet

Self-cleaning MOFs (CoBDC-NH_2)/GO nanofluidic membranes *via* interfacial cooperative assembly for high-performance wastewater treatment

Siyuan Chen[a], Hongjun Lin[a], Zhiyu Zhao[a], Cheng Chen[a], Wei Yu[a], Boya Wang[a], Jing Ma[a], Leihong Zhao[b], Guanhua Jin[c], Liguo Shen[a,*]

[a] College of Geography and Environmental Sciences, Zhejiang Normal University, Jinhua 321004, China
[b] College of Jewelry, Shanghai Jianqiao University, Shanghai 201306, China
[c] School of Energy and Chemical Engineering, Xinjiang Institute of Technology, Aksu 843100, China

ARTICLE INFO

Article history:
Received 7 June 2025
Revised 11 September 2025
Accepted 16 October 2025
Available online 16 October 2025

Keywords:
Metal-organic framework
Graphene oxide
Molecular sieving
Self-cleaning
XDLVO theory

ABSTRACT

Despite the compelling potential of metal-organic framework (MOF) membranes for water remediation, their poor membrane-forming crystallinity, limited solution-processability, and propensity to aggregate have impeded industrial deployment. Through interfacial cooperative assembly, we construct a well-dispersed 2D/3D nanofluidic composite membrane by coupling novel three-dimensional CoBDC–NH_2 nanocrystals (one-dimensional channels, 7 Å × 8.6 Å) with two-dimensional graphene oxide (GO). The synergistic interfacial interactions between flexible GO and rigid MOF components create a highly uniform architecture while furnishing rapid electron-transfer pathways and strong electrostatic repulsion; the rigid CoBDC–NH_2 imparts angstrom-scale molecular sieving, ultrafast water-transport channels, and catalytically active Co sites. This interfacial synergy delivers an exceptional pure-water flux of 737.5 L m^{-2} h^{-1} bar^{-1} together with 99.8 % rejection of bulky anionic dyes, decisively breaking the canonical flux-selectivity trade-off. XDLVO theory analysis confirms pronounced antifouling propensity, and density-functional-theory (DFT) calculations show that interfacial cooperative effects between GO and MOF lower the activation barrier for peroxymonosulfate (PMS) activation, enabling a self-cleaning cycle that restores 90.3 % of the initial flux after fouling. By integrating molecular-precision sieving, charge-regulated transport, and *in-situ* catalytic regeneration within a scalable platform *via* interfacial cooperative assembly, this work offers a versatile blueprint for next-generation high-performance MOF membranes and signals broad opportunities in sustainable wastewater treatment and beyond.

© 2026 Published by Elsevier B.V. on behalf of Chinese Chemical Society and Institute of Materia Medica, Chinese Academy of Medical Sciences.

Water pollution, especially organic pollution from industry, has seriously threatened human health and environmental safety [1–3]. Membrane separation technology, with its comprehensive advantages such as high selectivity, environmental friendliness and low operating costs, has become an effective way to control water pollution [4–7]. However, organic pollutants in water, especially industrial dyes, have complex components, wide sources and diverse properties, and are difficult to be treated by traditional membrane technology.

Fortunately, metal-organic framework (MOF), one of the molecular sieve materials, with its precisely adjustable pore structure, can provide strong dimensional exclusion and steric hindrance for dye retention while offer stable sub-nanometer channels for water molecules, which provides an efficient approach for separation of dyes-water mixture [8–11]. In practical applications, MOFs are usually loaded onto substrate membranes to address their own difficulty in dispersion and provide operational components for water treatment [12–14]. The loading methods typically include casting, *in-situ* growth, phase separation, *etc.* [15–17]. And the substrate films include polymer substrates, ceramic substrates, graphene substrates, *etc.* Among them, graphene oxide (GO) itself contains rich oxygen-containing groups [18–20], which can significantly improve the uniformity of MOF dispersion [21]. Through the interface collaborative assembly strategy, MOF and GO can form high-quality stacks that fill each other, enhancing the mechanical properties of the film and the stability of the MOF layer [22].

Inspired by the interfacial cooperative assembly concept, we propose an environmental-friendly strategy for synthesis of a novel three-dimensional MOF (CoBDC–NH_2, with a pore size of

* Corresponding author.
E-mail address: lgshen@zjnu.cn (L. Shen).

https://doi.org/10.1016/j.cclet.2025.111982
1001-8417/© 2026 Published by Elsevier B.V. on behalf of Chinese Chemical Society and Institute of Materia Medica, Chinese Academy of Medical Sciences.

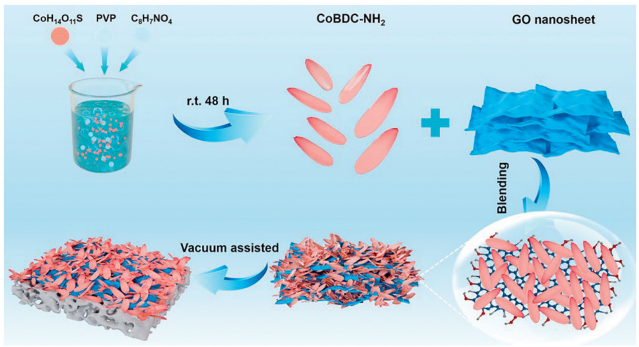


Fig. 1. Schematic diagram of the fabrication process of the $GO_xCoBDC–NH_2$ composite membrane *via* interfacial cooperative assembly.

7 Å × 8.6 Å) at room temperature, and present a 2D/3D nanofluidic GO-MOF composite membrane ($GO_{60}CoBDC–NH_2$) synthesizing by vacuum-assisted self-assembly (VASA) process (Fig. 1 and Text S1 in Supporting information) [23]. MOF grows on the uniform layered skeleton of GO, and the rigid channels provide precise dimensional sieving, resulting in an ultra-high-water flux of 737.5 L m^{-2} h^{-1} bar^{-1} and a retention rate of up to 99.8 % for various dye molecules. The charge transfer synergy between GO and the exposed Co sites of MOF can effectively activate peroxymonosulfate (PMS) to generate reactive oxygen species (ROS), *in-situ* degrading adhered organic matter and endowing the membrane with self-cleaning properties, resulting in a 90.3 % flux retention (without any treatment). The simple preparation strategy and excellent performance of $GO_{60}CoBDC–NH_2$ provide a feasible solution for water pollution treatment.

Firstly, we synthesized a brand-new MOF material (named $CoBDC–NH_2$) through a simple solvothermal self-assembly method (Text S2 in Supporting information). Single crystal X-ray diffraction (SC-XRD) (Text S4 in Supporting information) shows that the as-synthesized $CoBDC–NH_2$ crystallizes in the monoclinic system, space group $C2/c$, with cell parameters $a = 33.095$ Å, $b = 9.776$ Å, $c = 17.989$ Å, $\alpha = \gamma = 90°$, $\beta = 99.71°$, and $Z = 4$. Co^{2+} ions coordinate with the ditopic linker 2-aminoterephthalic acid (NH_2-BDC) to form the primary building block (Fig. S1a in Supporting information), which further assembles into a μ_3–O-bridged trinuclear $Co_3O(COO)_6$ secondary building unit (SBU, Fig. S1b in Supporting information). These SBUs are connected by organic linkers in a (6,2) mode, periodically extending into a three-dimensional framework with pts-like topology (Fig. S1c in Supporting information), clearly depicted in the node-and-link diagram (Fig. S1d in Supporting information). Along the *b* axis, the SBUs arrange in a periodic "bead-on-a-string" fashion, generating one-dimensional, nearly square channels that traverse the crystal (7 Å × 8.6 Å; Figs. S1e and S2 in Supporting information). Three-dimensional pore topology analysis (Fig. S1f in Supporting information) reveals that the main channels interconnect with lateral micro-pores, yielding a porosity of 47.8 %, a uniform pore size distribution, and a single diffusion pathway that underpin the material's excellent molecular-sieving capability. Scanning electron microscope (SEM) and transmission electron microscope (TEM) (Figs. S3a and S4a in Supporting information) show that translucent flake particles with a size of about 2 μm self-assemble into a loosely stacked layered network, which shortens the water transport pathway and improves mass transfer efficiency [24–26]. Energy dispersive X-ray spectroscopy (EDX) spectra (Figs. S3b and c in Supporting information) confirm the homogeneous distribution of C, O, N, and Co throughout the MOF, indicating homogeneous chemical composition. X-ray diffraction (XRD) (Fig. S3d in Supporting information) showed that the diffraction peaks were well matched to the simulation pattern, with no additional reflections, showing high crystallinity and structural integrity [27]. X-ray photoelectron spectroscopy (XPS) (Figs. S3e-h in Supporting information) identified C, O, N, and Co elements, with peaks of 284.6, 285.6, and 288.5 eV in C 1s attributed to C–C/C = C, C–O, and C = O bonds, and the presence of aromatic rings confirmed by low-intensity π-π^* satellite bands [28]. The peaks of 532.9, 531.5, and 531.2 eV in O 1s correspond to Co-O, C = O, and C–O bonds. The Co 2p spectrum showed the main peaks at 780.6 eV (Co $2p_{3/2}$) and 796.9 eV (Co $2p_{1/2}$) with distinct satellite peaks, indicating the coexistence of Co^{2+} and Co^{3+} [29]. These results verify the elemental composition of $CoBDC–NH_2$ and the valence state of the metal center.

Moreover, we exposed the $CoBDC–NH_2$ framework to acidic, alkaline and pure water, and no change in crystal structure was found after a period of time (Fig. S4b in Supporting information), indicating excellent water and acid and alkali resistance.

Then, $GO_xCoBDC–NH_2$ membranes were prepared by vacuum-assisted self-assembly (VASA) (Text S3 in Supporting information) [24]. The XRD (Text S4) results showed that the diffraction peaks of $GO_{60}CoBDC–NH_2$ were the same as those of $CoBDC–NH_2$ (5.4° and 10.9°) (Fig. S5a in Supporting information), and FT-IR results showed N–H tensile vibration (3311–3136 cm^{-1}) and aromatic C = C band (1530 cm^{-1}) in both $GO_{60}CoBDC–NH_2$ and $CoBDC–NH_2$ (Fig. S5b in Supporting information), indicating the integrity of the MOF structure during membrane formation. Notably, in $GO_{60}CoBDC–NH_2$, the -OH band (2896–3690 cm^{-1}) was significantly weakened, indicating the formation of hydrogen bonds between GO and $CoBDC–NH_2$ [30]. The XPS results showed that Co^{2+} was present in the composite membrane, but the Co^{3+} peak was stronger than that of MOF, indicating that the oxygen-containing functional group of GO interacted with Co^{2+} and led to its oxidation, which confirmed the important role of GO in regulating the chemical environment of the metal center (Figs. S5c-f in Supporting information) [31]. In addition, comparing Figs. S5d and e, Figs. S3f and g, and Fig. S6 (Supporting information), it was found that the C–C, C = O, and π-π^* signals in the composite membrane mainly came from organic ligands, while the O 1s signal was significantly stronger than that of organic ligands, indicating that the introduction of GO increased the oxygen-containing functional groups on the membrane surface and enhanced the chemical activity. Although the amount of graphene oxide is small, its high specific surface area and abundant surface functional groups significantly regulate the oxidation state of the metal center in $CoBDC–NH_2$ and improve the interfacial chemical activity of the composite membrane.

We used GO as the matrix phase and co-dispersed 5 mg of $CoBDC–NH_2$ crystals in deionized water (0, 20, 40 and 60 μg, named GO_0, GO_{20}, GO_{40} and GO_{60}) with different GO content (Fig. S7 in Supporting information). Subsequently, the mixed solution was filtered to the nylon support membrane through vacuum filtration, and the interface co-assembly of $CoBDC–NH_2$ and GO nanosheets was realized. As shown in Fig. 2a, GO in colloids provides steric hindrance and electrostatic repulsion to prevent agglomeration between MOF particles and achieve orderly packing [32]. As shown in Figs. 2b and d, Fig. S8 (Supporting information), there are almost no surface defects observed on $GO_{60}CoBDC–NH_2$, while the opposite is true for $CoBDC–NH_2$. The atomic force microscope (AFM) results showed that the former had a lower surface roughness, which further confirmed the effectiveness of this method in the synthesis of dense films (Figs. 2c and e). The EDX results showed that the homogeneous distribution of C, O, N and Co matched the $CoBDC–NH_2$ composition, confirming the homogeneity of the structure (Figs. 2f and g). In addition, $GO_{60}CoBDC–NH_2$ has good flexibility (Fig. 2h). And the small increase in water contact angle (WCA) indicated that the compact surface partially inhibits the ingress of water, but the

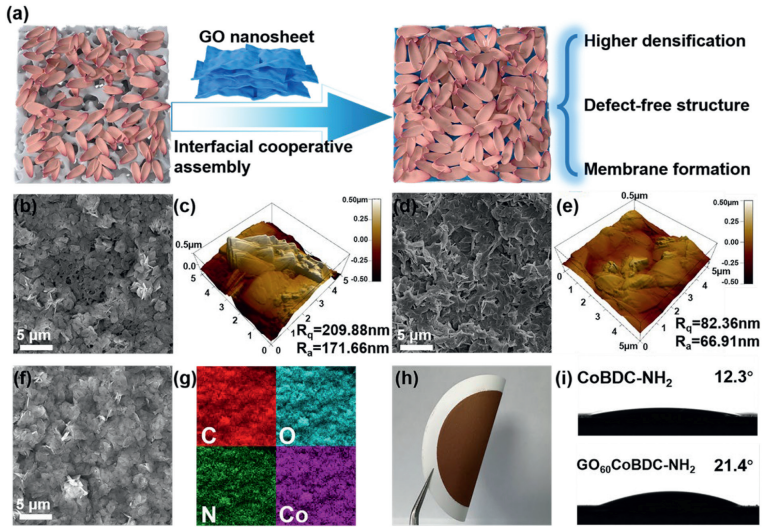


Fig. 2. Interfacial cooperative assembly and multiscale structural characterization of the GO_xCoBDC–NH_2 composite membrane. (a) Schematic of the interfacial cooperative assembly fabrication process. (b) SEM image of CoBDC–NH_2. (c) AFM of CoBDC–NH_2. (d) SEM image of GO_{60}CoBDC–NH_2. (e) AFM of GO_{60}CoBDC–NH_2. (f, g) EDX of GO_{60}CoBDC–NH_2. (h) Optical photograph of GO_{60}CoBDC–NH_2. (i) Water-contact-angle images of CoBDC–NH_2 and GO_{60}CoBDC–NH_2.

flake CoBDC–NH_2 still provides a rapid diffusion channel for water molecules (Fig. 2i).

Further wettability experiments (Fig. S9 in Supporting information) showed that when GO was not present, CoBDC–NH_2 membrane delivered a pure water flux (PWF) as high as 4365.3 L m^{-2} h^{-1} bar^{-1}, because abundant through-going defects between MOF particles formed low-resistance water pathways. When the GO content increases to 60 μg, the GO_{60}CoBDC–NH_2 membrane exhibiting a PWF of 790.65 L m^{-2} h^{-1} bar^{-1} (Fig. S9a). This is due to GO nanosheets facilitated interfacial cooperative assembly by inserting into the micropores and voids of CoBDC–NH_2, promoting intimate integration between adjacent crystals and sealing defect channels. The corresponding increase in the water contact angle from 12.3° to 21.4° (Fig. S9b) can be attributed to the fact that the graphene oxide matrix partially masks the hydrophilic site of the MOF during the interfacial co-assembly process, and the wettability is weakened due to the reduction of surface roughness (Fig. S9c).

We performed permeation and rejection tests with 20 ppm brilliant blue G (BBG) as the model dye (Text S5 in Supporting information). As shown in Fig. 3a, when GO content increasing from 0 μg to 60 μg, BBG rejection rose sharply from 79.6 % to 99.5 %, demonstrating a substantial enhancement in separation selectivity, which can be attributed to size-sieving effect and electrostatic repulsion (Fig. 3d). GO acts as a flexible adhesive that binds the MOF particles, creating denser pores, and thereby strengthening exclusion of large dye molecules. GO_{60}CoBDC–NH_2 membrane carries a much higher negative surface charge density than the CoBDC–NH_2 membrane (zeta-potential measurements, Fig. S10 in Supporting information), generating stronger electrostatic repulsion against the anionic dye BBG and further boosting rejection. Furthermore, GO_{60}CoBDC–NH_2 membrane can handle not only for BBG but also other dyes with different molecular structures (Fig. S11 in Supporting information) and charge properties (Table S1 in Supporting information).

As shown in Fig. 3b, the macromolecular anionic dye Congo red (CR) was almost completely blocked, with a rejection of 99.8 %. However, small molecule dyes, such as crystal violet (CrV), partially penetrate the membrane, but the treatment effect of GO_{60}CoBDC–NH_2 membrane is still significantly higher than that of CoBDC–NH_2 membrane. Notably, while sustaining high rejection, the GO_{60}CoBDC–NH_2 membrane maintains an outstanding water flux of 605.6 L m^{-2} h^{-1} bar^{-1}, outperforming most reported analogues in overall separation efficiency (Fig. 3f). Moreover, the membrane possessed 99 % BBG rejection and stable flux in complex feed matrices tap water, river water, lake water, and secondary effluent from a wastewater-treatment plant (Fig. 3c and Fig. S12 in Supporting information) and exhibited excellent tolerance across wide pH and ionic-strength ranges (Fig. S13 in Supporting information). The operational stability was initially confirmed through ten filtration cycles, where no discernible decline in performance was observed (Fig. S14 in Supporting information). Crucially, to verify its long-term durability under continuous operation, a 24-h cross-flow filtration test was conducted. During this extended period, the flux gradually stabilized at a high level of $>$ 400 L m^{-2} h^{-1} bar^{-1}, while the rejection rate remained excellent at approximately 98 % (Fig. 3e). These combined results strongly confirm the structural stability and long-term applicability of the membrane in high-flux dye-separation scenarios.

In addition, we analyzed the pressure-flux relationship of GO_{60}CoBDC–NH_2 membrane (Fig. S15 in Supporting information), and the results showed that the flux was linearly correlated with the pressure before 2 bar, and the growth rate of flux slowed down after 2 bar, indicating progressive membrane compaction that narrowed and densified the mass-transfer channels.

We investigated the process by which membrane-activated PMS produces ROS (Fig. 4a) [33–35]. When the PMS does not exist, GO_{60}CoBDC–NH_2 and pure CoBDC–NH_2 membranes removed 16.5 % and 11.3 % of MB during 30 min operation. And once 20 mg of PMS was added, MB removal ratio separately increased to 89.8 % and 100 % of pure CoBDC–NH_2 membranes and GO_{60}CoBDC–NH_2 membranes. This not only indicates that the activation of PMS to produce ROS improves the separation performance, but also indicates that GO promotes the activation of PMS. To further investigate activation stability, an MB degradation experiment was performed over 10 cycles with 360 min per cycle (Fig. 4b). The results showed that PMS catalytic performance of GO_{60}CoBDC–NH_2 membrane has maintained stable after multiple rounds. In addition, initial pure water flux (J_{water}), post-contamination flux (J_{dye}), recovery flux by pure water rinsing ($J_{rinsing}$), and recovery flux by PMS activation (J_{PMS}) were evaluated sequentially (Fig. 4c). Flux of the CoBDC–NH_2 membrane can be restored to 88.9 % by water rinsing, indicating that flux of the membranes cannot be fully restored by water flushing alone. Contrastively, flux of GO_{60}CoBDC–NH_2 mem-

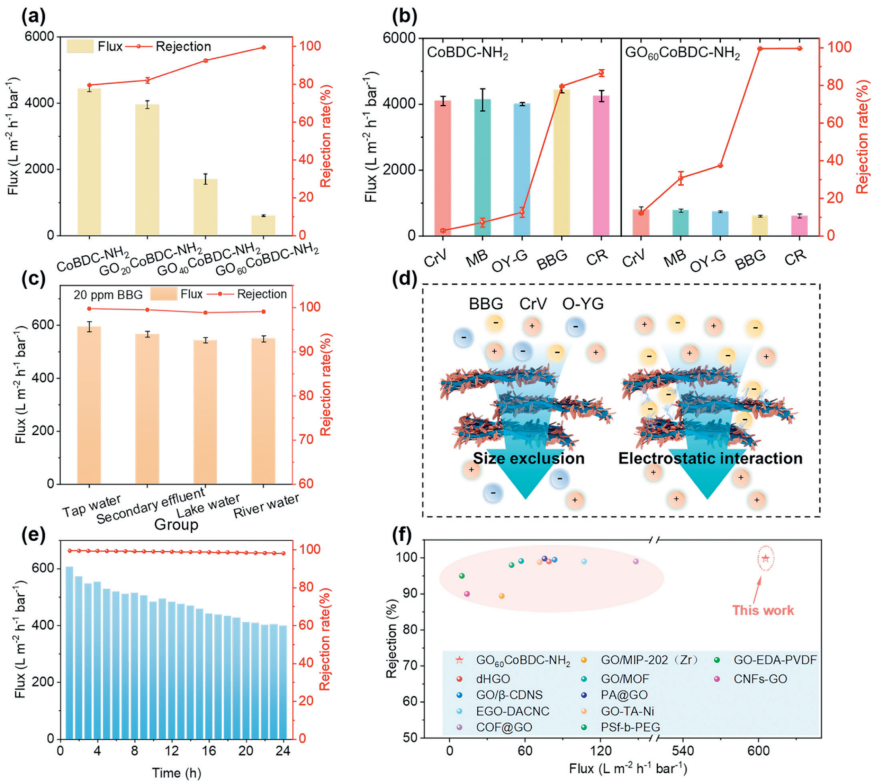


Fig. 3. Separation performance of the $GO_xCoBDC–NH_2$ membranes. (a) Water flux and BBG rejection of $GO_xCoBDC–NH_2$ membranes at 20 ppm BBG. (b) Flux and rejection for various 20 ppm dyes on $CoBDC–NH_2$ and $GO_{60}CoBDC–NH_2$ membranes. (c) Rejection by the $GO_{60}CoBDC–NH_2$ membrane in real-water matrices. (d) Schematic illustration of the separation mechanism of the $GO_{60}CoBDC–NH_2$ membrane. (e) The long-term stability during the separation process. (f) Comparison of BBG rejection and water permeance of the $GO_{60}CoBDC–NH_2$ membrane with previously reported membranes (Table S2 in Supporting information).

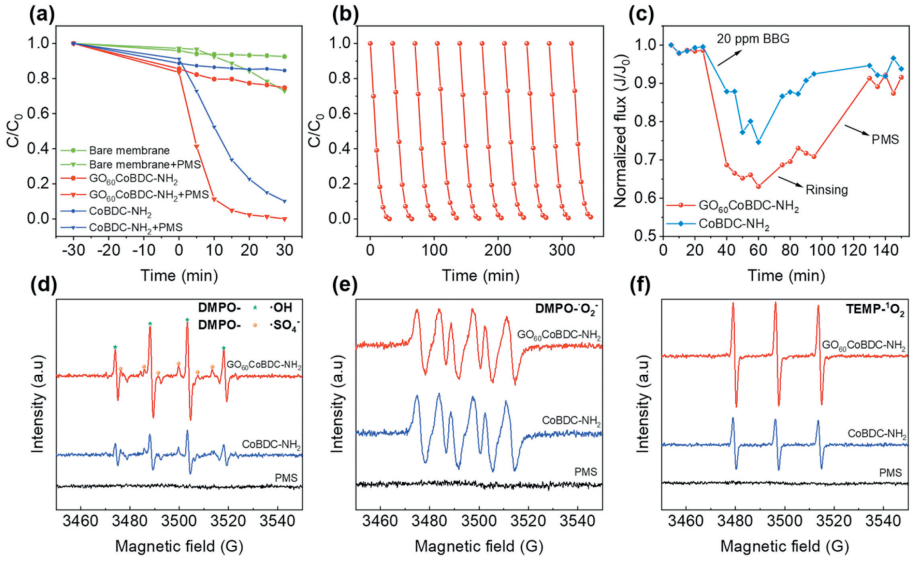


Fig. 4. (a) Degradation curves of methylene blue (MB) in different systems. (b) Catalytic degradation cycle tests of $GO_{60}CoBDC–NH_2$ membranes. (c) Normalized flux over time during filtration of BBG solution with $CoBDC–NH_2$ and $GO_{60}CoBDC–NH_2$ membranes, electron paramagnetic resonance (EPR) spectra of (d) DMPO-·OH, (e) DMPO-$^{\cdot}O_2^-$ and (f) DMPO-$^1O_2$.

brane can be restored to 90.3 % after 30 min of PMS treatment, which was significantly better than water rinsing and faster than $CoBDC–NH_2$ membrane. The $GO_{60}CoBDC–NH_2$ membrane exhibits excellent and sustainable self-cleaning ability in the presence of PMS.

The *in-situ* EPR (Figs. 4d-f) confirms the generation of ·OH, $^{\cdot}SO_4^-$, $^{\cdot}O_2^-$ and $^1O_2$, they were involved in the PMS activation reaction [36–39], providing multiple oxidation pathways for dye degradation. It is worth noting that the EPR signal intensity of various free radicals in $GO_{60}CoBDC–NH_2$ membrane is significantly stronger, suggest that GO greatly facilitates the efficient generation of ROS [40]. And the degradation effect of methylene blue was significantly reduced when specific scavengers were introduced to capture ·OH, $^{\cdot}SO_4^-$, $^{\cdot}O_2^-$ and $^1O_2$, indicating that the above-mentioned ROS played a leading role in the dye degradation process (Fig. S16 in Supporting information). In addition, we present a

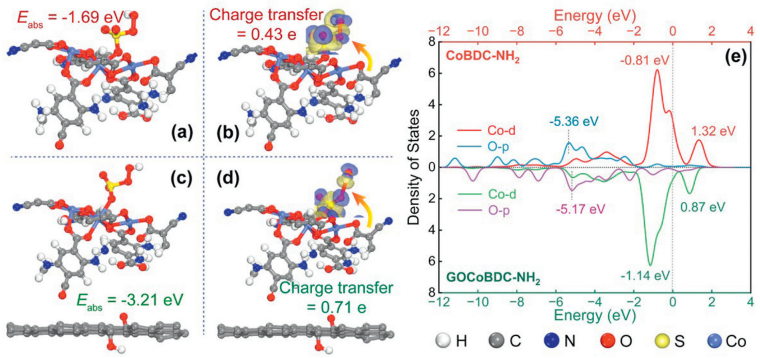


Fig. 5. Adsorption conformation (a) and charge density (b) of CoBDC–NH_2 with PMS. Adsorption conformation (c) and charge density (d) of GO_{60}CoBDC–NH_2 with PMS, blue area indicates electron accumulation while yellow area indicates depletion. Electronic state density of Co and O atoms (e).

model of the relevant reaction mechanism (Fig. S17 in Supporting information): PMS activation → ROS generation → *in-situ* decomposition of organic → flux recovery and separation efficiency maintenance, which can be represented by the equations listed in Text S6 (Supporting information).

Density-functional-theory (DFT) calculations (Text S7 and Fig. S18 in Supporting information) indicate that the sulfur atoms in PMS and the oxygen atoms in MOF form chemical bonds. As shown in Figs. 5a-d, the significant reduction in adsorption energy (−1.69 eV *vs.* −3.21 eV) suggests a markedly enhanced adsorption affinity of GO_{60}CoBDC–NH_2 for PMS. More charge transfer (0.43e *vs.* 0.71e) indicates that GO_{60}CoBDC–NH_2 can activate PMS more effectively. The p electronic distribution of O in the GO_{60}CoBDC–NH_2 is at a shallower position (Fig. 5e, −5.36 eV *vs.* −5.17 eV).

XDLVO theory analysis (Table S3 and Text S8 in Supporting information) shown that negative total interaction energy between pure GO membrane and the fouling indicated that the two were thermodynamically attracted, while both the CoBDC–NH_2 membrane and the GO_{60}CoBDC–NH_2 membrane exhibited positive total interfacial interaction energies during filtration, indicating significant thermodynamic repulsion (Figs. S19a-c in Supporting information). Moreover, the CoBDC–NH_2 membrane had the highest pollutant repulsion barrier and showed the strongest anti-fouling ability, while the GO_{60}CoBDC–NH_2 membrane had a slightly lower total rejection energy but still maintained a strong repulsion ability (Fig. S19d in Supporting information). Although GO slightly reduces the repulsion energy barrier, GO_{60}CoBDC–NH_2 membrane still maintains high fouling resistance comparable to that of CoBDC–NH_2 membrane overall.

In summary, we successfully developed a defect-free composite membrane (GO_{60}CoBDC–NH_2) through interfacial cooperative assembly of novel three-dimensional nanocrystals with two-dimensional GO nanosheets. The synergistic interfacial interactions between flexible GO and rigid MOF components create a highly uniform membrane structure, where GO facilitates rapid electron transport pathways and strong electrostatic repulsion, while CoBDC–NH_2 imparts sub-nanometer molecular sieving capabilities and ultra-fast water transport channels with exposed catalytically active cobalt sites. The resulting composite membrane achieves an outstanding pure water flux of 737.5 L m^{-2} h^{-1} bar^{-1} and efficiently retains large-volume anionic dyes, such as CR, with a retention rate of 99.8 %, effectively overcoming the typical flux-selectivity trade-off in membrane separation. XDLVO analysis indicates a positive interfacial energy barrier between the membrane surface and pollutants, confirming the superior anti-fouling properties. While DFT calculations indicate the critical cooperative interfacial interplay GO and MOF, which enhances electron transfer during PMS activation, markedly increasing the generation rate of ROS, enabling highly efficient self-cleaning performance and achieving over 90.3 % recovery of the initial flux post-fouling. By integrating simple, eco-friendly, and scalable fabrication techniques, this work achieves simultaneous advancements in molecular sieving and self-cleaning performance through interfacial cooperative assembly, establishing a robust platform for MOF-based membranes in water purification and offering innovative perspectives for designing next-generation multifunctional separation systems.

Declaration of competing interest

The authors declare that they have no known competing financial interests or personal relationships that could have appeared to influence the work reported in this paper.

CRediT authorship contribution statement

Siyuan Chen: Writing – original draft, Methodology, Investigation. **Hongjun Lin:** Writing – review & editing, Project administration, Funding acquisition. **Zhiyu Zhao:** Methodology, Investigation. **Cheng Chen:** Methodology, Investigation. **Wei Yu:** Methodology, Investigation. **Boya Wang:** Methodology, Investigation. **Jing Ma:** Methodology, Investigation. **Leihong Zhao:** Methodology, Investigation. **Guanhua Jin:** Methodology, Investigation. **Liguo Shen:** Supervision, Project administration, Funding acquisition.

Acknowledgments

This work was financially supported by "Pioneer" and "Leading Goose" R&D Program of Zhejiang (Nos. 2024C03124, 2025C04049 and 2025C02240), Zhejiang Provincial Outstanding Youth Science Foundation (No. LR22E080007), National Natural Science Foundation of China (No. 52070170) and "Tianchi Talents" Program of Xinjiang.

Supplementary materials

Supplementary material associated with this article can be found, in the online version, at doi:10.1016/j.cclet.2025.111982.

References

[1] K. Islam, K. Maeno, R. Yokoi, et al., Science 387 (2025) 1214–1218.
[2] I. Elouafi, Science 387 (2025) 6563.
[3] B.W. Brooks, Environ. Sci. Technol. Lett. 12 (2025) 356–357.
[4] C. Du, W. Liu, Environ. Int. 190 (2024) 108858.
[5] M.S. Denny, J.C. Moreton, L. Benz, S.M. Cohen, Nat. Rev. Mater. 1 (2016) 16078.
[6] Y.H. Jin, M.H. Li, Y.W. Yang, Adv. Sci. 12 (2025) 2412600.
[7] Z. Zhang, H. Fu, Z. Wang, et al., Adv. Sustain. Syst. 8 (2024) 2300597.
[8] P. Cheng, Y. Huang, C. Wu, et al., J. Membr. Sci. 640 (2021) 119812.
[9] B. Li, H.M. Wen, Y. Cui, et al., Adv. Mater. 28 (2016) 8819–8860.

[10] Y.V. Kaneti, J. Tang, R.R. Salunkhe, et al., Adv. Mater. 29 (2017) 1604898.
[11] Z. Jiang, L. Wang, W. Xue, et al., Sep. Purif. Technol. 328 (2024) 125025.
[12] X. Zheng, L. Chen, H. Zhang, et al., Angew. Chem. Int. Ed. 62 (2023) e202216710.
[13] X. Li, Y. Liu, J. Wang, et al., Chem. Soc. Rev. 46 (2017) 7124–7144.
[14] S.J. Datta, A. Mayoral, N. Murthy Srivatsa Bettahalli, et al., Science 376 (2022) 1080–1087.
[15] Y. Mu, X. Pei, Y. Zhao, et al., Nano Mat. Sci. 5 (2023) 351–360.
[16] W. Feng, C. Liu, Z. Liu, H. Pang, Chin. Chem. Lett. 35 (2024) 109552.
[17] X. Liu, T. Yue, K. Qi, et al., Chin. Chem. Lett. 31 (2020) 2189–2201.
[18] Z. Wang, B. Mao, M. Zhao, et al., ACS Nano 16 (2022) 3934–3942.
[19] F. Deng, T. Zhao, X. Zhang, et al., Chin. Chem. Lett. 36 (2025) 109897.
[20] M. Zhu, Y. Liu, M. Chen, et al., Chin. Chem. Lett. 31 (2020) 2683–2688.
[21] A. Knebel, A. Bavykina, S.J. Datta, et al., Nat. Mater. 19 (2020) 1346–1353.
[22] L. Mao, H. Park, R.A. Soler-Crespo, et al., Nat. Commun. 10 (2019) 3677.
[23] Z. Lin, Z. Han, G.E.P. O'Connell, et al., Adv. Mater. 36 (2024) 2312797.
[24] Z. Wang, N. Li, L. Zong, J. Zhang, Curr. Opin. Solid State Mater. Sci. 23 (2019) 142–148.
[25] M.S. Khan, S. Zhu, T.S. Chung, S.B. Chen, Chem. Eng. J. 515 (2025) 163730.
[26] S. Zou, A. Hammad, J. Huang, et al., Chin. Chem. Lett. 37 (2026) 111619.
[27] Y. Liu, Y. Wang, B. Sengupta, et al., Adv. Mater. 37 (2025) 2417994.
[28] M.C. Biesinger, Surf. Interface Anal. 49 (2017) 1325–1334.
[29] H. Cao, L. Shi, Z. Xiong, et al., Adv. Mater. 37 (2025) 2414362.
[30] Q. Guo, X.F. Yu, K. Zhang, et al., App. Catal. B: Environ. 343 (2024) 123581.
[31] W. Zhang, B. Yang, Z. Xiang, Chin. Chem. Lett. 36 (2025) 109630.
[32] L. Feng, K.Y. Wang, G.S. Day, et al., Chem. Rev. 120 (2020) 13087–13133.
[33] M.d.J. Velásquez-Hernández, R. Ricco, F. Carraro, et al., Cryst. Eng. Comm. 21 (2019) 4538–4544.
[34] X. He, Z. Wu, J. Lu, et al., Small 20 (2024) 2402589.
[35] Z.J. Xiao, B.Q. Zhou, X.C. Feng, et al., App. Catal. B: Environ. 328 (2023) 122483.
[36] H. Zhang, L. Lyu, Q. Fang, et al., App. Catal. B: Environ. 286 (2021) 119912.
[37] W. Zhang, S. Zhang, C. Meng, Z. Zhang, App. Catal. B: Environ. 322 (2023) 122098.
[38] P. Cai, J. Zhao, X. Zhang, et al., App. Catal. B: Environ. 306 (2022) 121091.
[39] P. Li, Y. Lin, Q. Huang, et al., App. Catal. B: Environ. 302 (2022) 120850.
[40] L. Qin, H. Ye, C. Lai, et al., App. Catal. B: Environ. 317 (2022) 121704.